Supplementary Information to Multi-Reward Reinforcement Learning Based Parameterization of Inter-atomic Potential Models for Silica

Aditya Koneru[1,2], Henry Chan[1,2], Sukriti Manna[1,2], Troy D. Loeffler[1,2], Debdas Dhabal[3], Andressa A Bertolazzo[3], Valeria Molinero[3], and Subramanian KRS Sankaranarayanan[1,2]

[1]Department of Mechanical and Industrial Engineering, University of Illinois,Chicago, Illinois 60607, United States
[2]Center for Nanoscale Materials, Argonne National Laboratory, Lemont, Illinois 60439, United States
[3]Department of Chemistry, The University of Utah, Salt Lake City, Utah 84112, United States
† E-mail: valeria.molinero@utah.edu
† E-mail: skrssank@uic.edu

June 18, 2023

Supplementary Note 1: Evolution of the best objective Scores

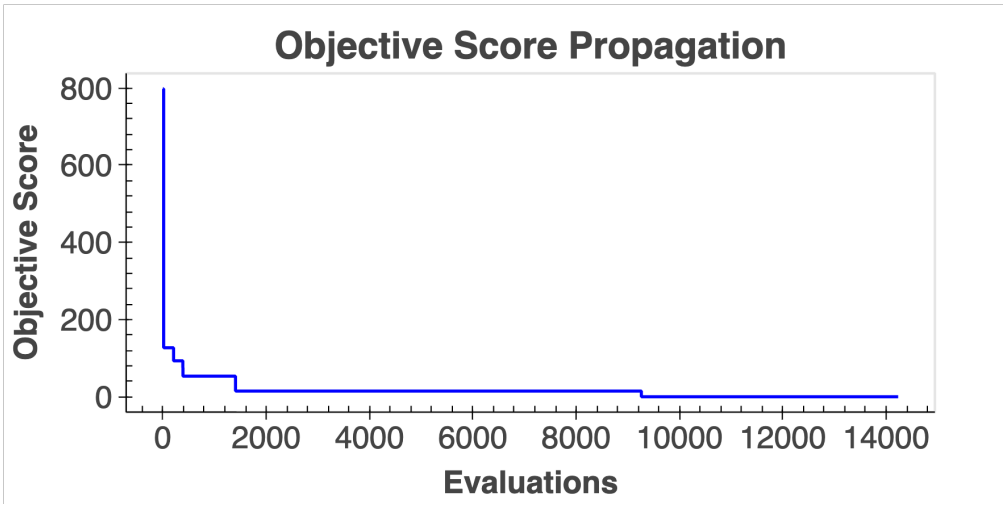

Supplementary Figure 1: MCTS Objective Score Evolution

One of the more successful versions of RL involves the use of Monte Carlo tree search (MCTS), which utilizes playouts to select the best possible action (with maximum reward) from the current state. Here, playouts refer to random actions from the model that allow it to learn by interacting with the environment. The larger the number of playouts, the better the model estimate of reward and the more promising is the model action selection. Notably, the MCTS performs this search in a tree structure, continuously growing either those leaves of the tree that result in a maximum reward (exploitation) or those which have not been

adequately sampled (exploration). The upper confidence bound (UCB) selection policy enables a search agent to balance between these exploratory and exploitative actions within the tree search. When we scan the continuous potential energy surface, a global search without good starting points can be a tedious process, especially owing to the fact we have limited information about the bounds of the search for most of the parameters. Here, the exploratory part of the policy allows us to search and set good starting points to exploit, thus enable us to reach optimal solutions without much initial input from the user. Moreover, once a parameter set is computed, it remains constant and we can reuse the score without recomputing. This combined with the simple arithmetic and customizable form of UCB makes it suitable for our iterative search. However, we need a good number of evaluations and also need to strike a balance between exploratory and exploitative modes by tuning the 'exploration constant'. Furthermore, our hierarchical objective evaluation method alleviates this problem by providing stage-wise rewards and reducing the number of evaluations. It is important to understand that when the action space is discrete, a parent leaf will exhibit finite possible child leaves, all (or some) of which can be assessed for their prominence. When the action space is continuous, the number of possible child leaves is infinite, irrespective of the depth of the parent leaf, making the use of MCTS seemingly impossible in continuous action space. Our modifications to the MCTS algorithm as discussed in [1] allow us to operate the MCTS algorithm in continuous search spaces such as, for example, the force-field parameter optimization.

As mentioned in the methods section, there is an exploration constant (as in equation 6) that was set to 100. Additionally, the tree depth was limited to 7 while the number of playouts and head expansion were set to 10 and 5 respectively.

Supplementary Note 2: Comparing the Objective Scores

The objective scores were computed for the existing models as in Figure 2 in order to compare against the ML-BKS. The objective score evolution of the best set has been presented in Figure 1. The scores were normalised with respect to the lowest score for simplicity.

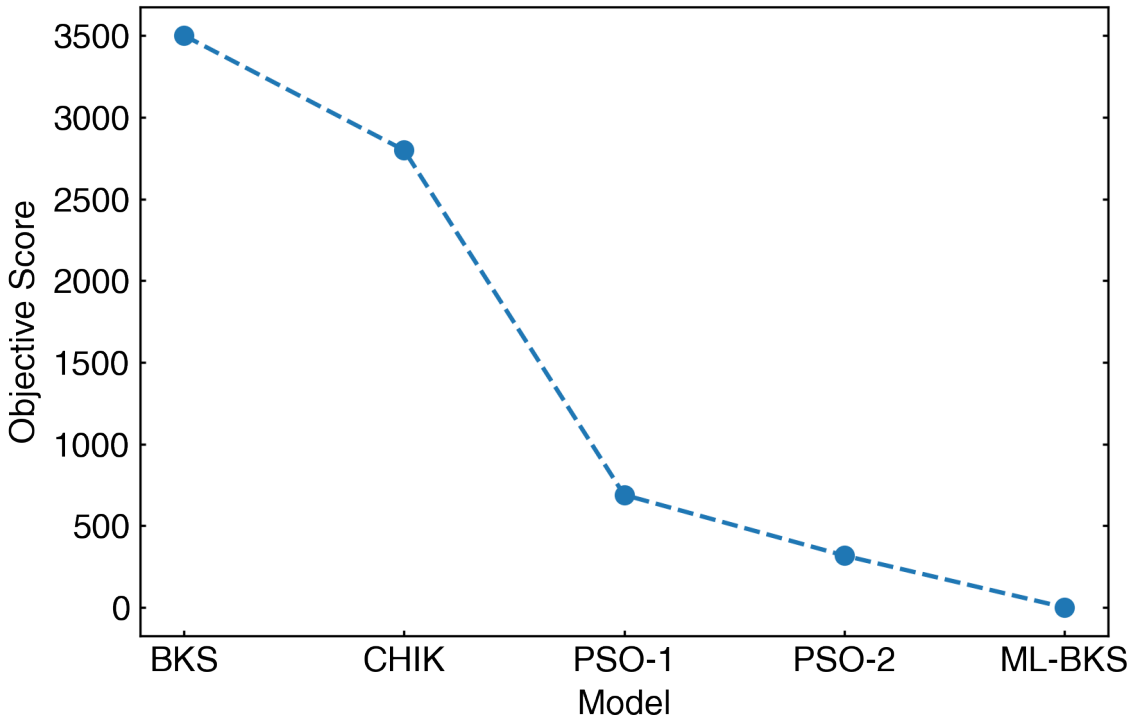

Supplementary Figure 2: Objective Scores computed using the scoring system for the existing force-fields and ML-BKS

Supplementary Table 1: Additional ML-BKS Parameters from this work

$Model$	A_{Si-Si}	ρ_{Si-Si}	C_{Si-Si}	A_{O-O}	ρ_{O-O}	C_{O-O}	A_{Si-O}	ρ_{Si-O}	C_{Si-O}	$q(Si)$
ML-BKS-1	3891	0.30	523.19	736.2	0.353	7.18	16554.90	0.1612	1.95	1.78
ML-BKS-2	3091	0.210	528.53	606.67	0.40	47.85	36547	0.176	133	2.3

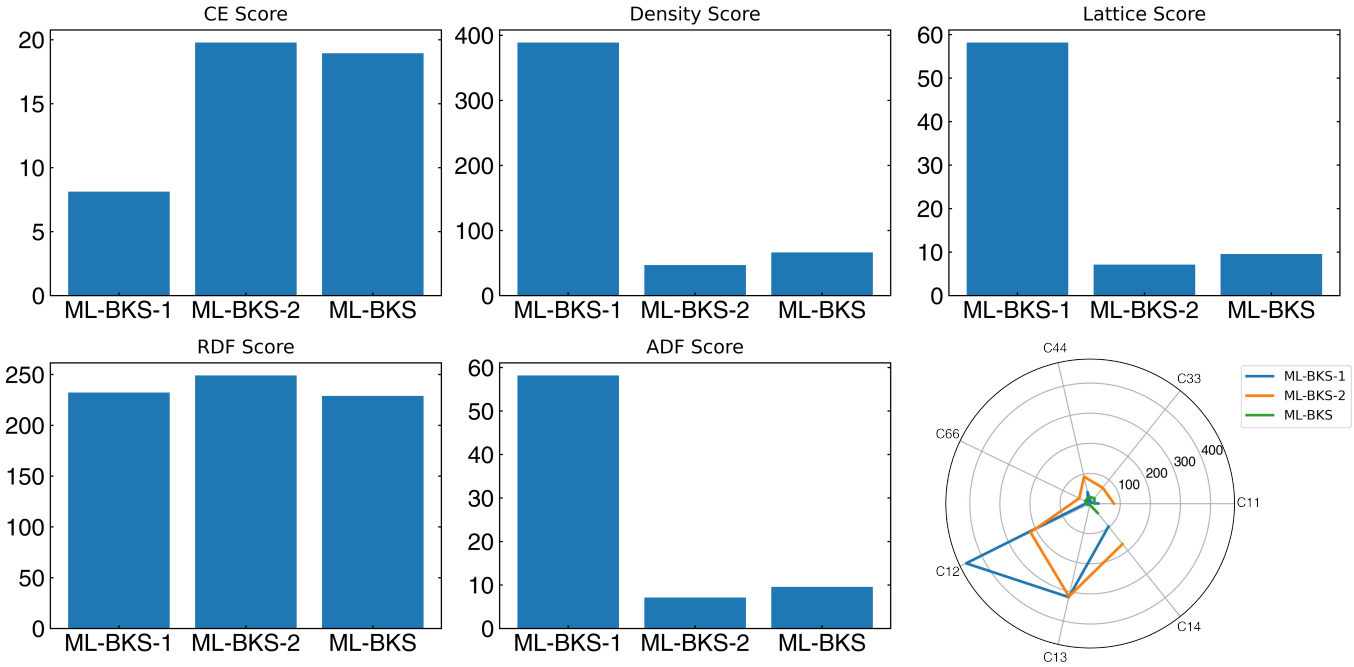

Supplementary Figure 3: Stage-wise scores compared between the best sets with the last subplot depicting the test property of each set

Supplementary Note 3: Amorphous silica modelled by ML-BKS-Solids

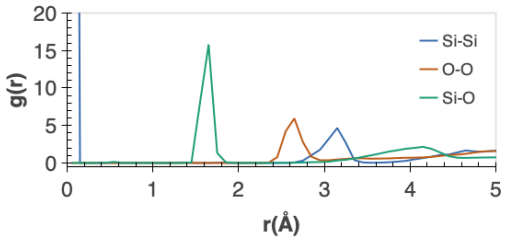

Supplementary Figure 4: Radial Distribution Function of the configuration prior to the failure of ML-BKS-Solids suggesting that lower Si-Si interatomic distances are being sampled by the model leading to catastrophic failure.

The amorphous silica when modelled using ML-BKS-Solids results in unphysical forces at much lower

temperatures than the melting point, proving the inability to capture high temperature dynamics.

Supplementary Note 4: Phonon Dispersions

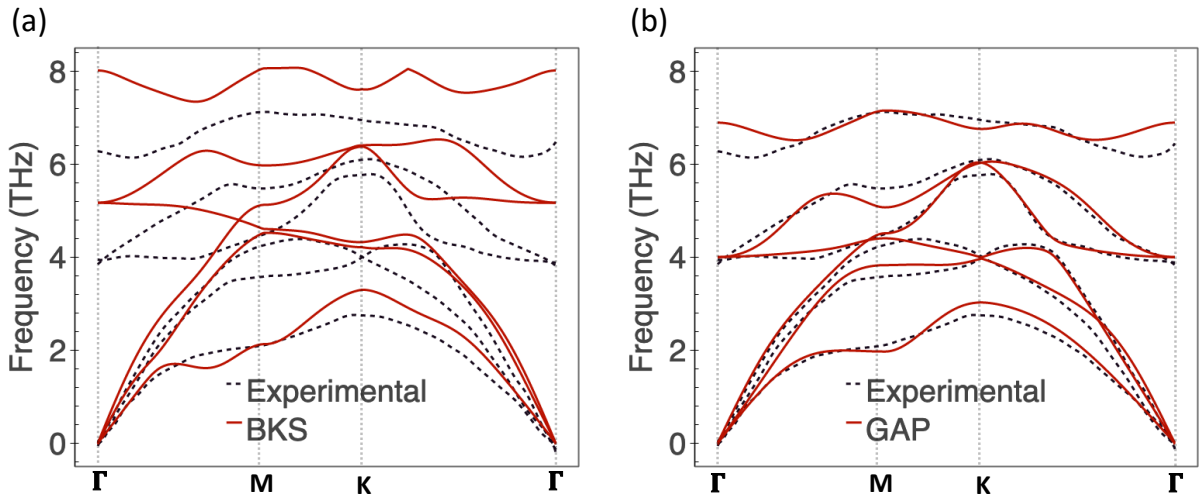

Supplementary Figure 5: phonon dispersion of BKS, GAP

Supplementary Note 5: Cell Parameter Comparisons

Supplementary Table 2: Comparison of Lattice Parameters between Experimental and ML-BKS Predictions

Polymorph	**a (Å)**		**b (Å)**		**c (Å)**		**alpha**		**beta**		**gamma**	
	Expt.	**ML-BKS**	**Expt.**	**ML-BKS**	**Expt.**	**ML-BKS**	**Expt.**	**ML-BKS**	**Expt.**	**ML-BKS**	**Expt.**	**ML-BKS**
Quartz	4.92	4.95	4.92	4.95	5.41	5.45	90.0	90.0	90.0	90.0	120.0	120.0
Cristobalite	4.97	4.98	4.97	4.98	6.92	6.94	90.0	90.0	90.0	90.0	90.0	90.0
Tridymite	18.52	18.63	5.00	5.03	23.81	23.94	90.0	90.0	105.8	105.8	90.0	90.0
Moganite	8.75	8.83	4.88	4.92	10.73	10.83	90.0	90.0	90.2	90.2	90.0	90.0
FER	18.71	19.12	14.07	14.38	7.42	7.58	90.0	90.0	90.0	90.0	90.0	90.0
AFI	13.59	13.90	13.59	13.90	8.43	8.62	90.0	90.0	90.0	90.0	120.0	120.0
MFI/F	20.26	20.18	19.90	19.83	13.25	13.20	90.0	90.0	90.0	90.0	90.0	90.0
MEL	20.10	20.38	20.10	20.38	13.35	13.53	90.0	90.0	90.0	90.0	90.0	90.0
MTW	25.03	25.61	5.15	5.27	11.87	12.14	90.0	90.0	109.3	109.3	90.0	90.0
CFI	13.57	14.03	5.12	5.29	25.23	26.09	90.0	90.0	90.0	90.0	90.0	90.0
STT	13.08	13.16	21.91	22.03	13.61	13.68	90.0	90.0	102.9	102.9	90.0	90.0
BEA	12.56	12.75	12.56	12.75	26.03	26.43	90.0	90.0	90.0	90.0	90.0	90.0
IFR	18.67	18.70	13.47	13.49	7.65	7.66	90.0	90.0	102.3	102.3	90.0	90.0
ITE	20.52	20.58	9.69	9.72	19.79	19.85	90.0	90.0	90.0	90.0	90.0	90.0
MWW	14.22	14.48	14.22	14.48	24.90	25.35	90.0	90.0	90.0	90.0	120.0	120.0
EMT	17.36	17.35	17.36	17.35	28.31	28.30	90.0	90.0	90.0	90.0	120.0	120.0
AST	13.23	13.64	13.23	13.64	13.23	13.64	90.0	90.0	90.0	90.0	90.0	90.0
CHA	13.57	13.73	13.57	13.73	14.66	14.83	90.0	90.0	90.0	90.0	120.0	120.0
FAU	24.26	24.51	24.26	24.51	24.26	24.51	90.0	90.0	90.0	90.0	90.0	90.0
MEI	13.26	13.16	13.26	13.16	15.73	15.62	90.0	90.0	90.0	90.0	120.0	120.0
ISV	12.78	13.05	12.78	13.05	25.50	26.02	90.0	90.0	90.0	90.0	90.0	90.0

Supplementary Note 6: Effect of Cut-off on ML-BKS Predictions

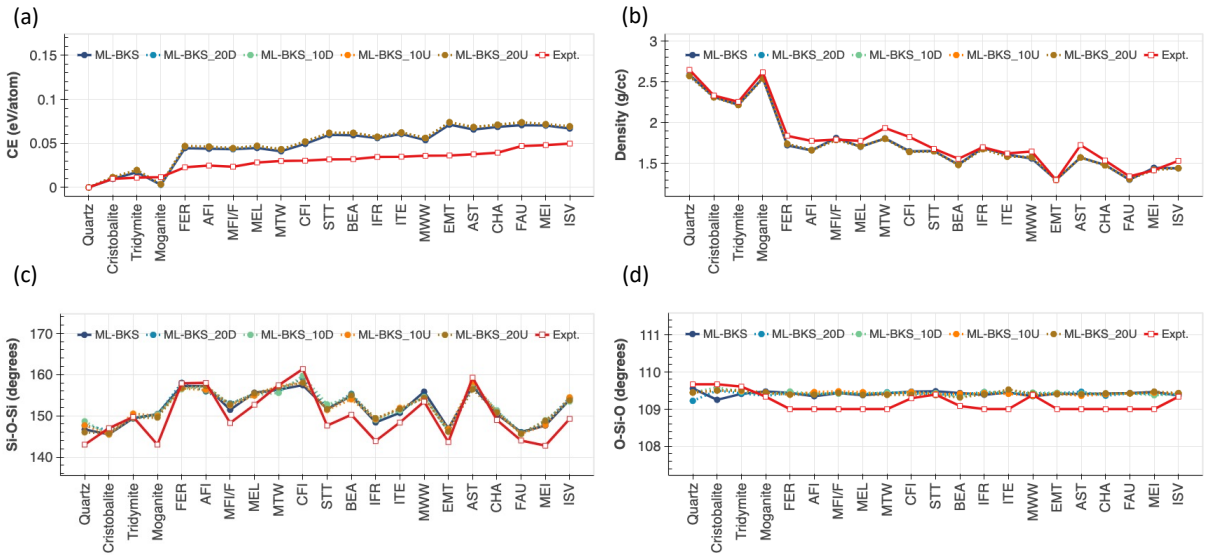

Supplementary Figure 6: Comparison of select properties and structural features of silica polymorphs predicted by different models. (a) Relative cohesive energy with respect to α-quartz, (b) Density, (c) Si-O-Si angle, (d) O-Si-O angle. All the properties were computed at 300K in order to compare with the reference experimental values. ML-BKS is the model developed in this work. The variation in pair-wise cut-off parameters by +10 percent, +20 percent, -10 percent and -20 percent are labeled as ML-BKS_10U and ML-BKS _20U, ML-BKS_10D, and ML-BKS_20D respectively.

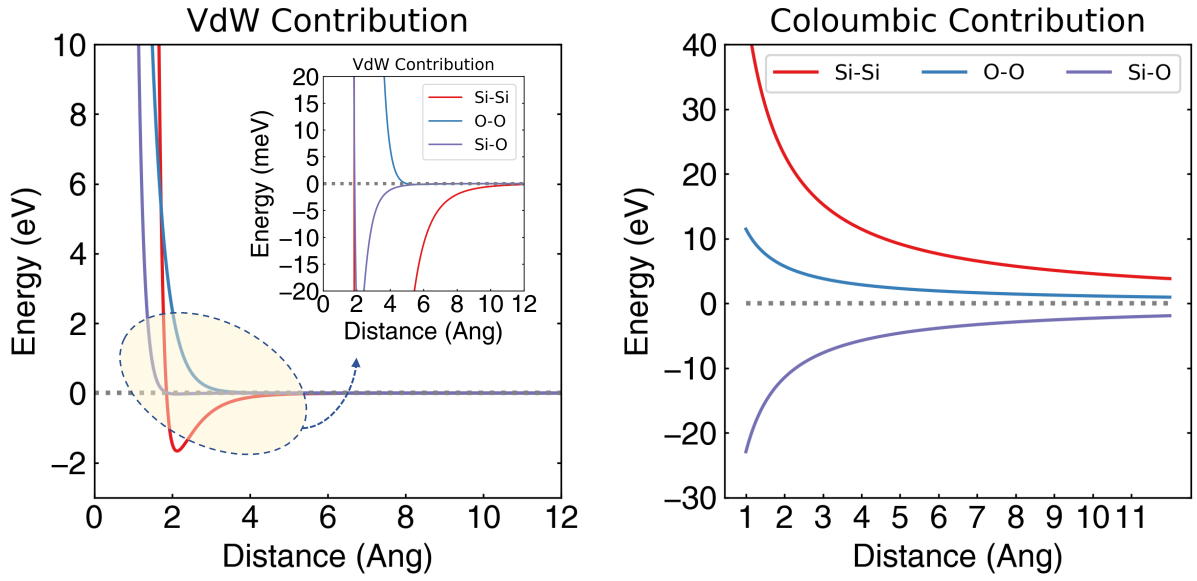

Supplementary Figure 7: VdW and Coloumbic contributions

Supplementary Note 7: Comparing Si-O and Si-O-Si between experiments and ML-BKS predictions

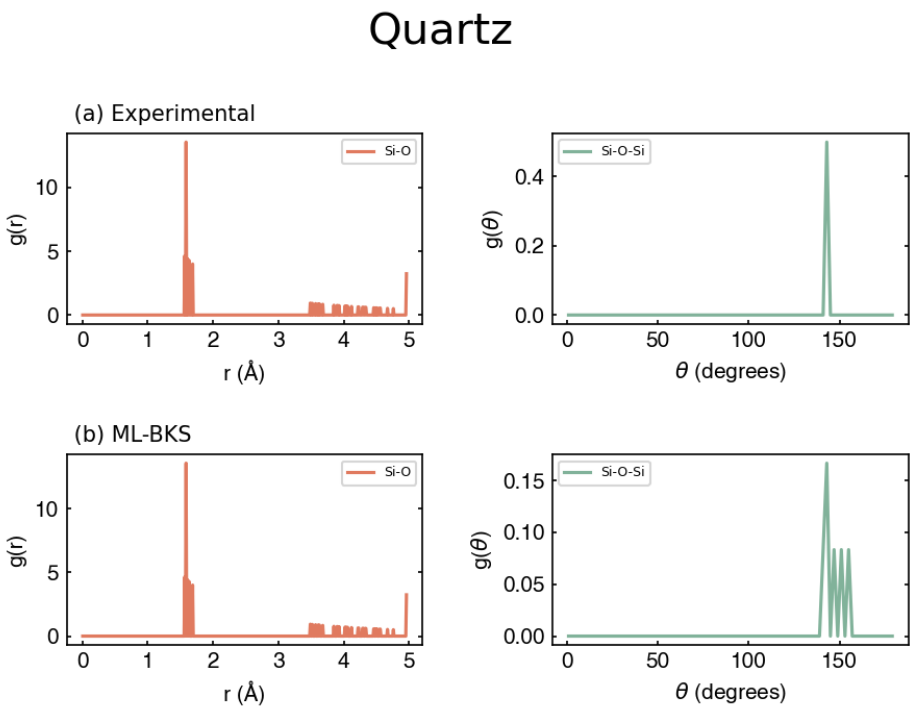

Supplementary Figure 8: Comparison of Si-O Bond Distance and Si-O-Si angle distribution from experiments and ML-BKS predictions for Quartz

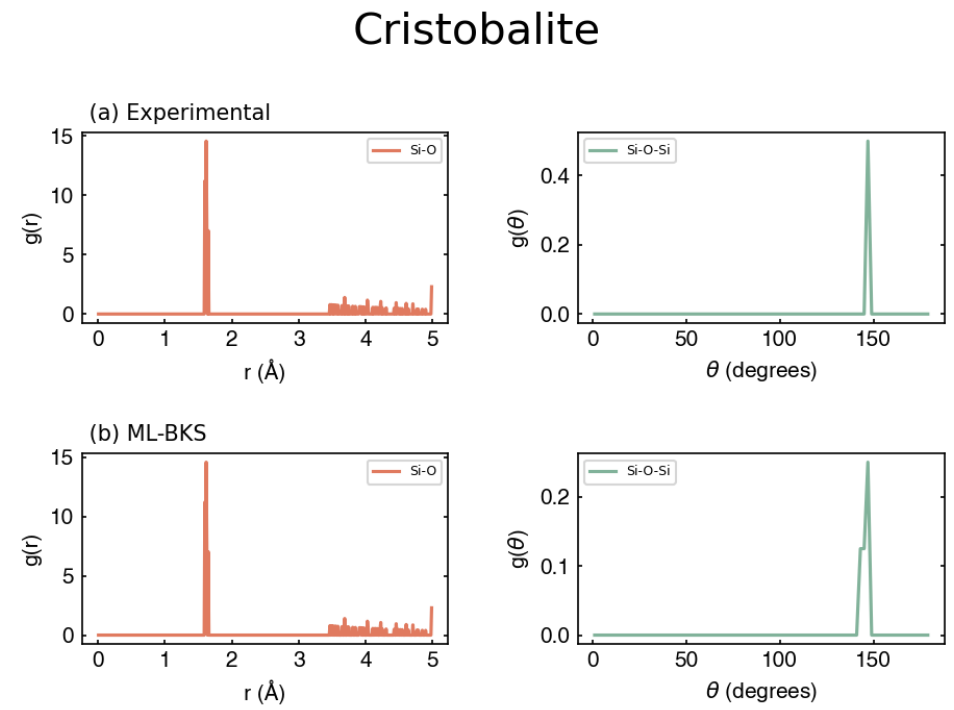

Supplementary Figure 9: Comparison of Si-O Bond Distance and Si-O-Si angle distribution from experiments and ML-BKS predictions for Cristobalite

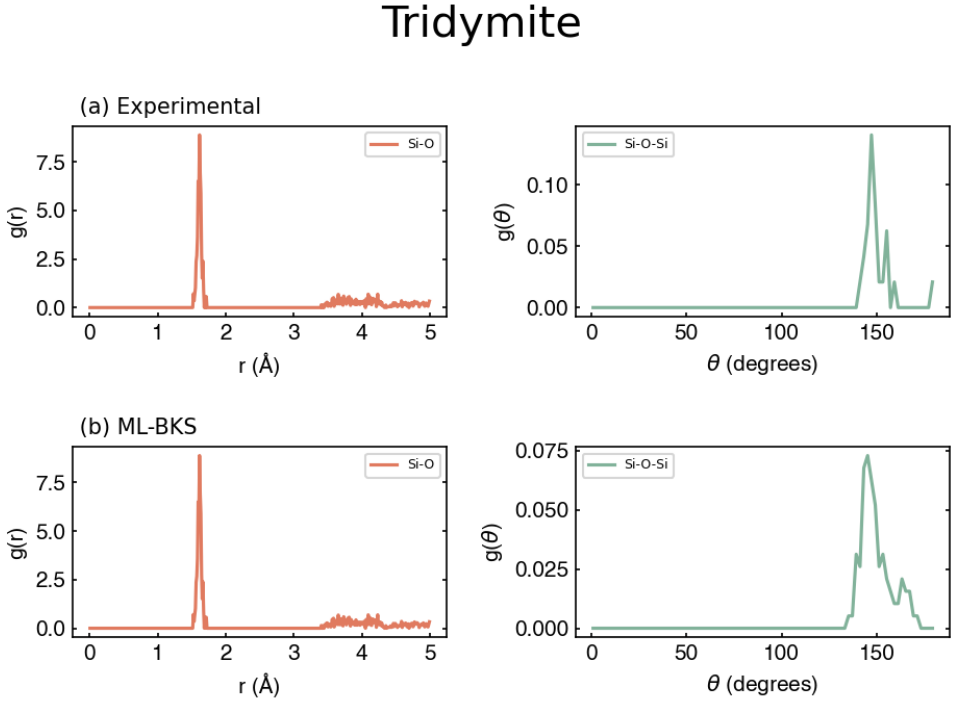

Supplementary Figure 10: Comparison of Si-O Bond Distance and Si-O-Si angle distribution from experiments and ML-BKS predictions for Tridymite

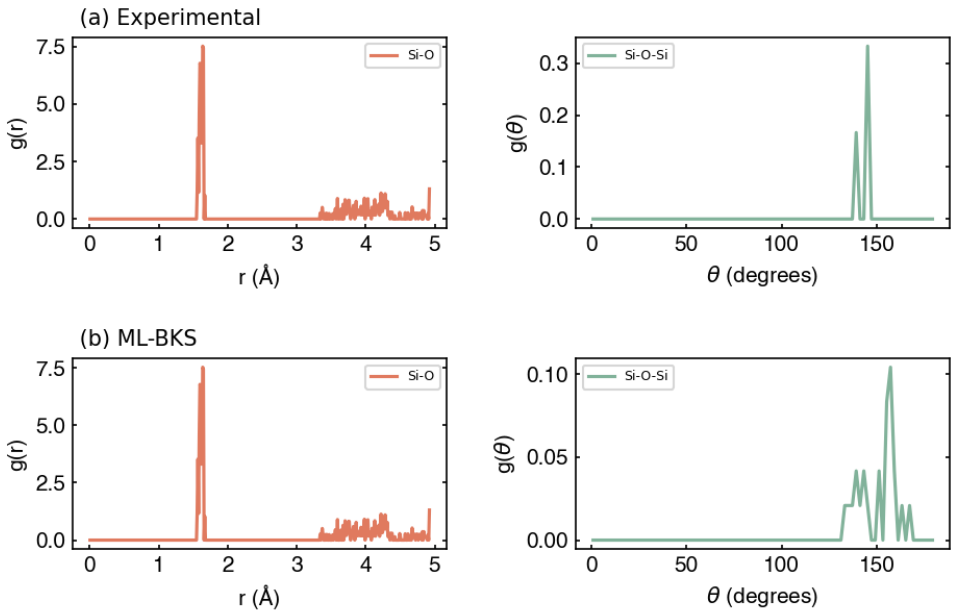

Supplementary Figure 11: Comparison of Si-O Bond Distance and Si-O-Si angle distribution from experiments and ML-BKS predictions for Moganite

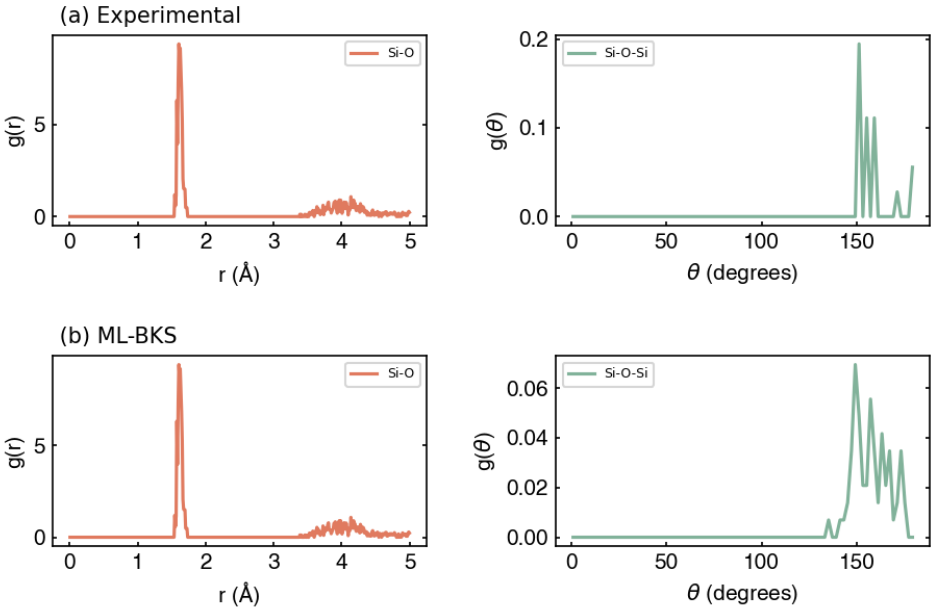

Supplementary Figure 12: Comparison of Si-O Bond Distance and Si-O-Si angle distribution from experiments and ML-BKS predictions for FER

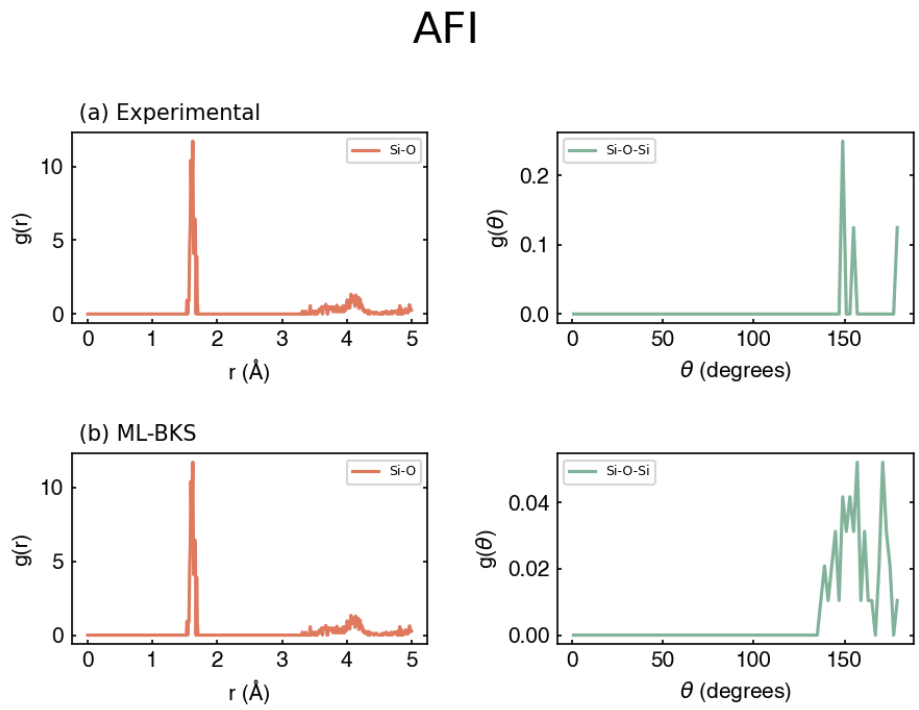

Supplementary Figure 13: Comparison of Si-O Bond Distance and Si-O-Si angle distribution from experiments and ML-BKS predictions for AFI

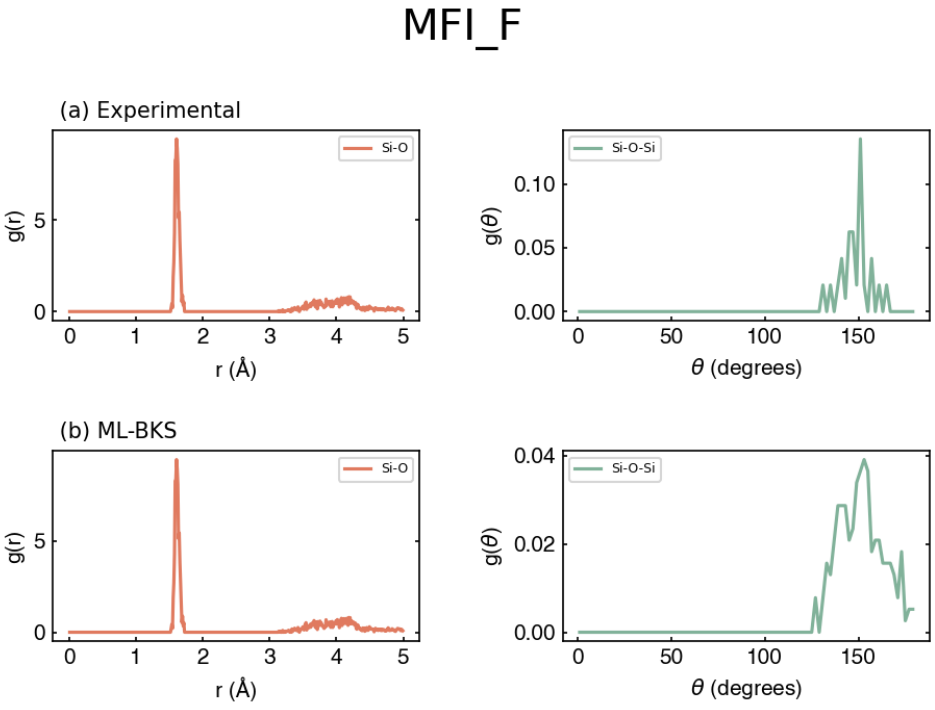

Supplementary Figure 14: Comparison of Si-O Bond Distance and Si-O-Si angle distribution from experiments and ML-BKS predictions for MFI_F

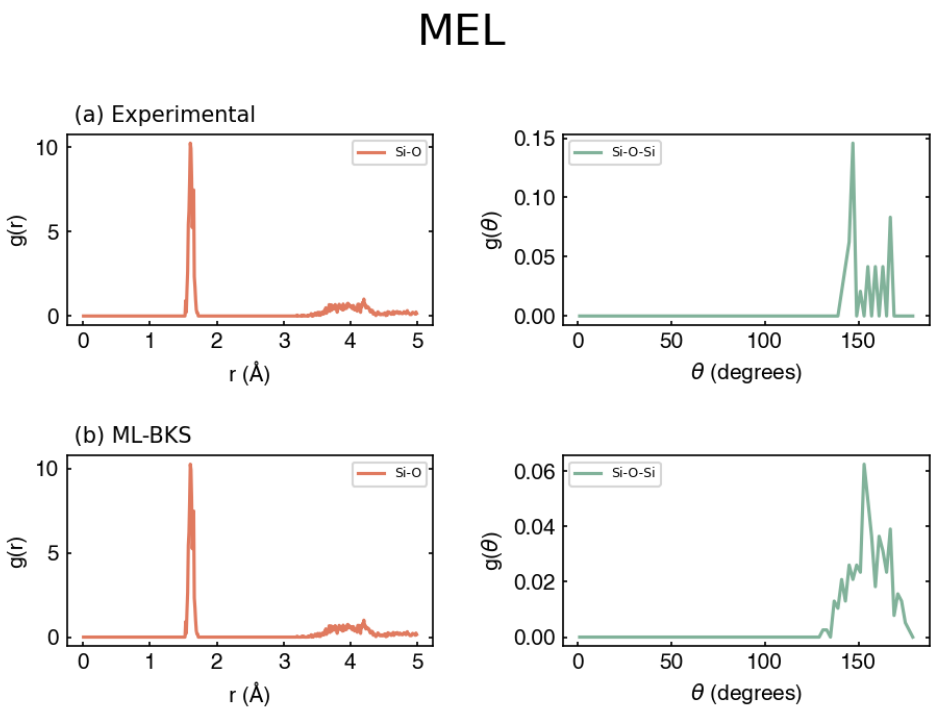

Supplementary Figure 15: Comparison of Si-O Bond Distance and Si-O-Si angle distribution from experiments and ML-BKS predictions for MEL

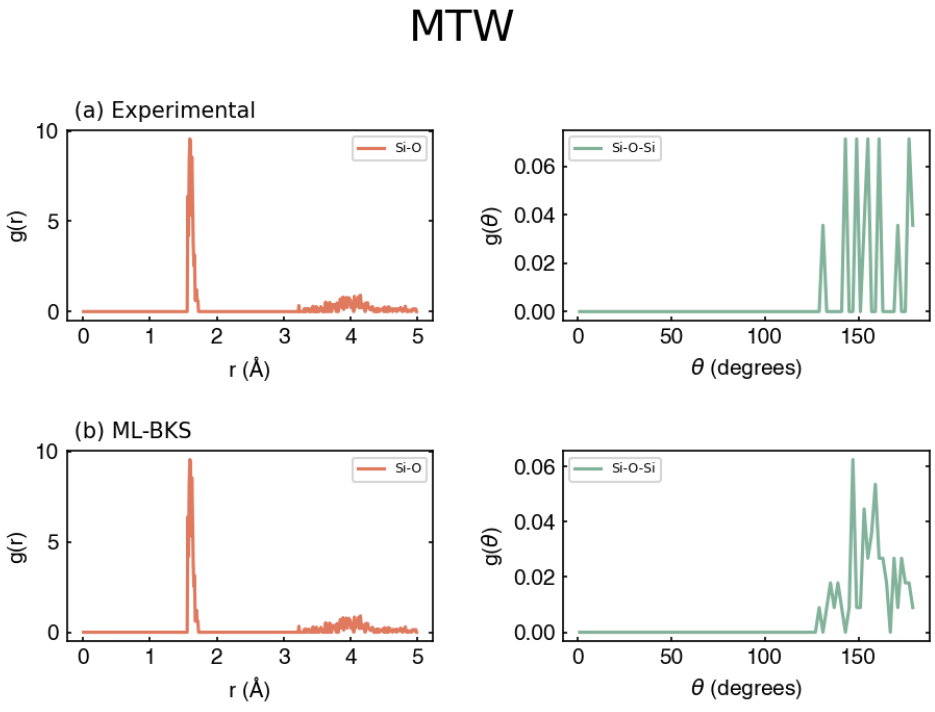

Supplementary Figure 16: Comparison of Si-O Bond Distance and Si-O-Si angle distribution from experiments and ML-BKS predictions for MTW

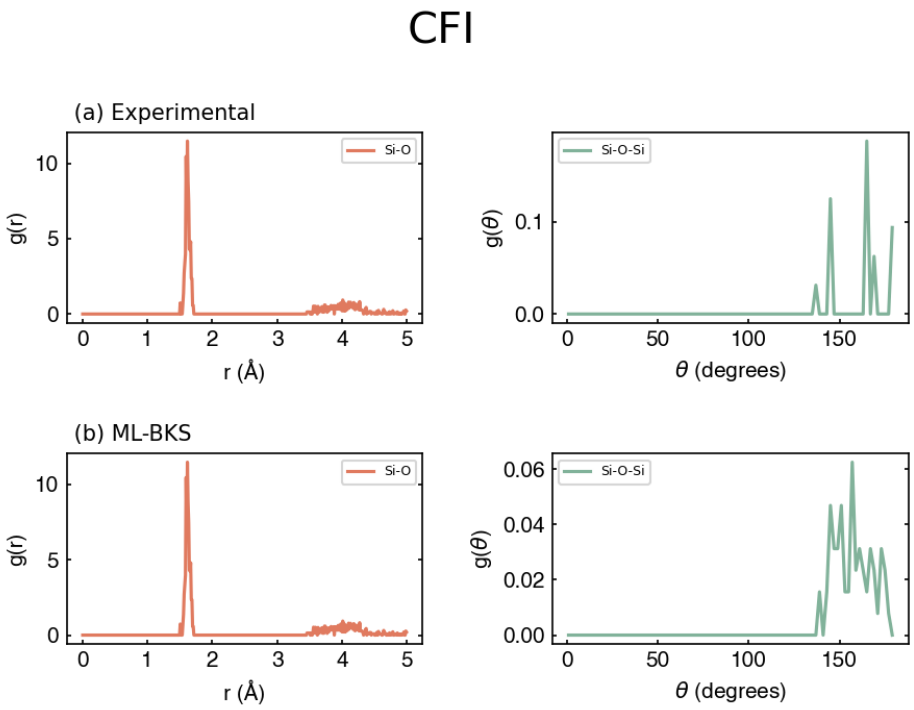

Supplementary Figure 17: Comparison of Si-O Bond Distance and Si-O-Si angle distribution from experiments and ML-BKS predictions for CFI

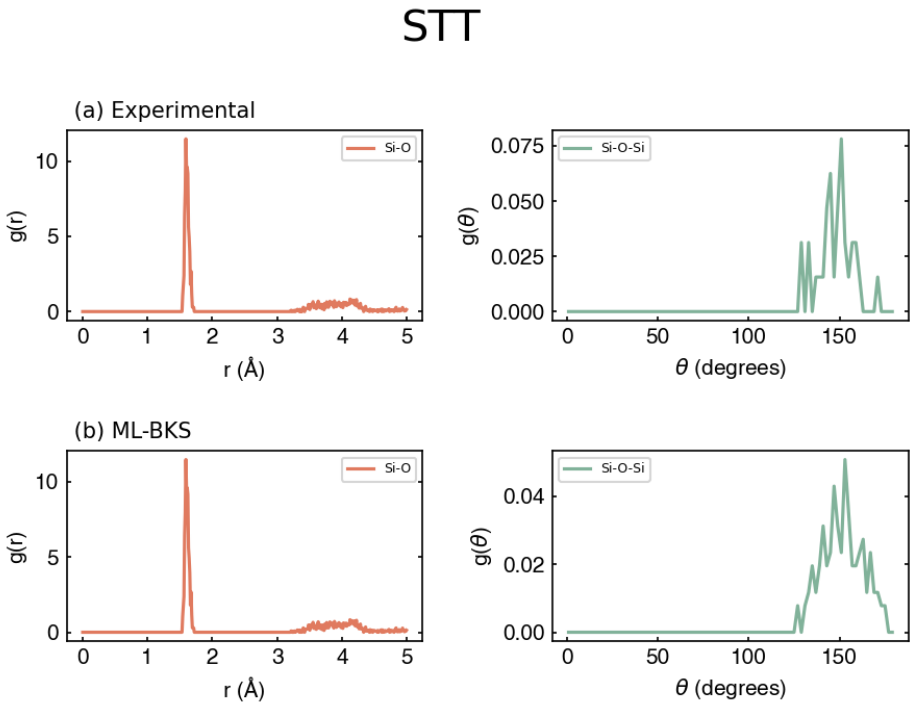

Supplementary Figure 18: Comparison of Si-O Bond Distance and Si-O-Si angle distribution from experiments and ML-BKS predictions for STT

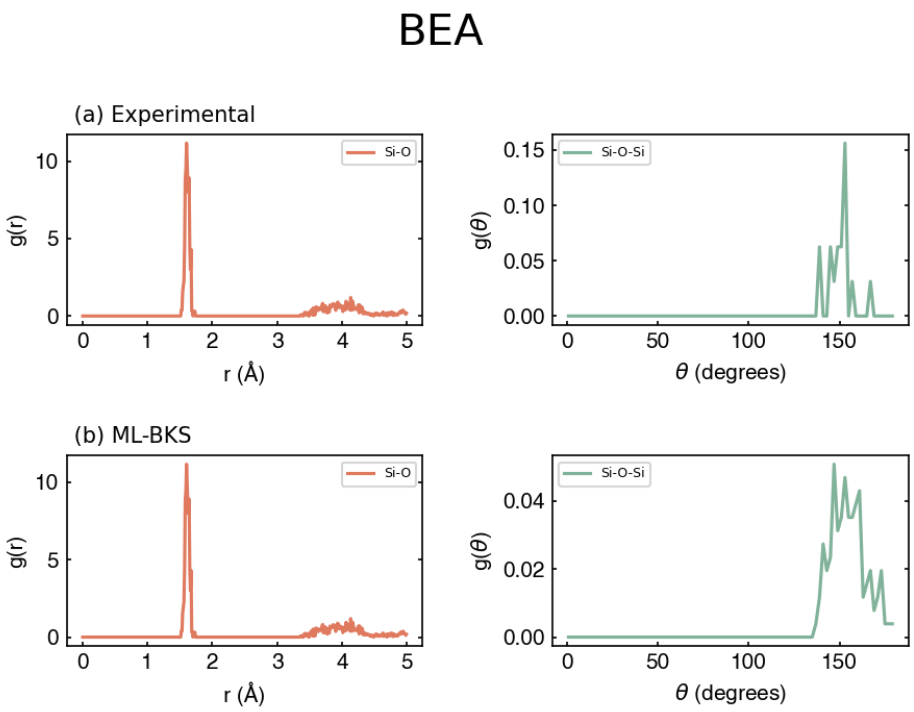

Supplementary Figure 19: Comparison of Si-O Bond Distance and Si-O-Si angle distribution from experiments and ML-BKS predictions for BEA

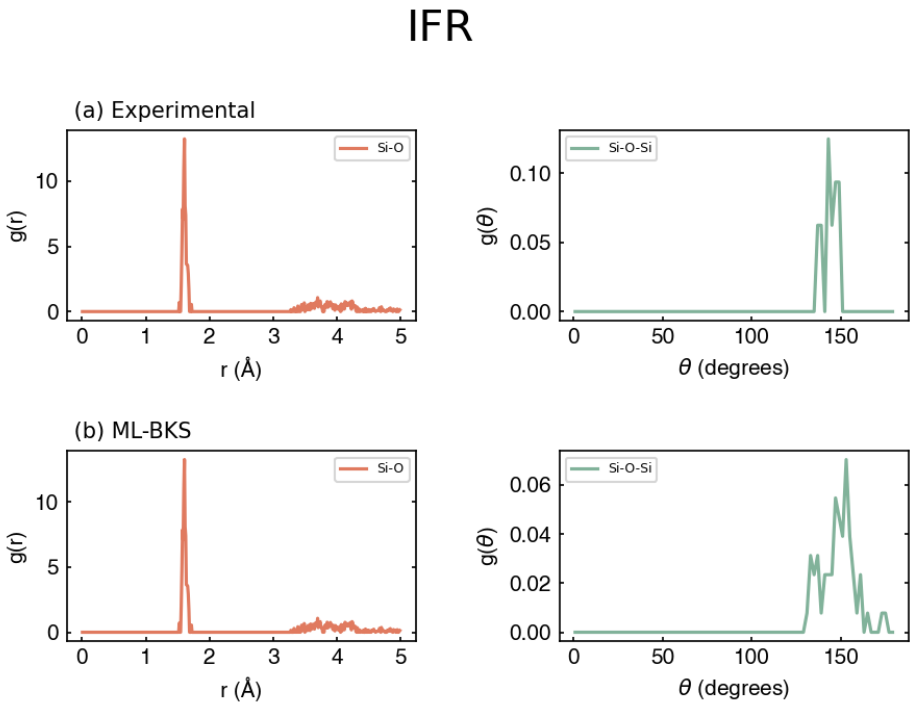

Supplementary Figure 20: Comparison of Si-O Bond Distance and Si-O-Si angle distribution from experiments and ML-BKS predictions for IFR

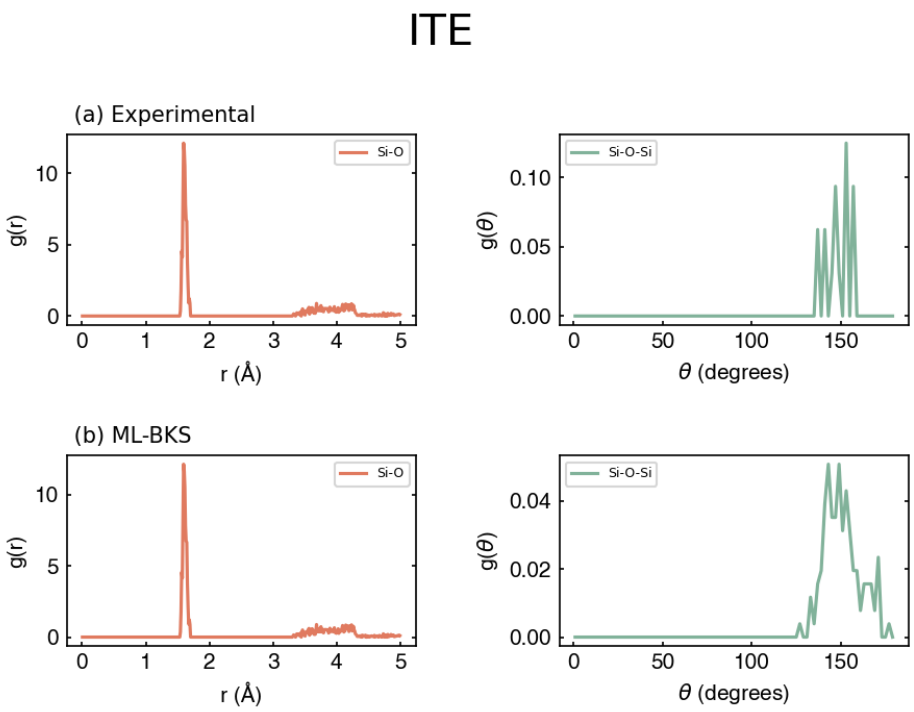

Supplementary Figure 21: Comparison of Si-O Bond Distance and Si-O-Si angle distribution from experiments and ML-BKS predictions for ITE

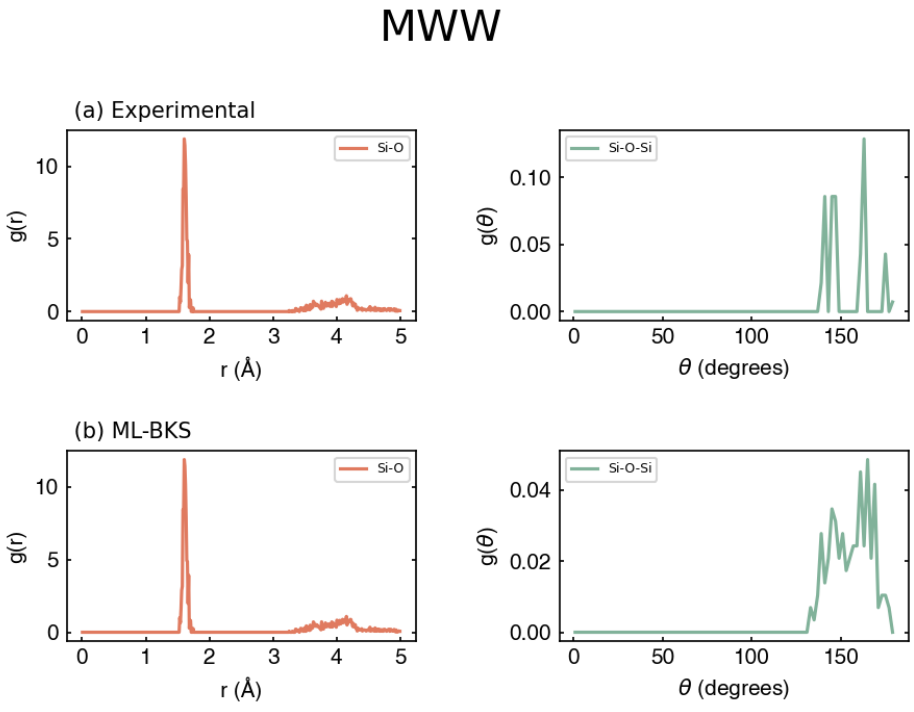

Supplementary Figure 22: Comparison of Si-O Bond Distance and Si-O-Si angle distribution from experiments and ML-BKS predictions for MWW

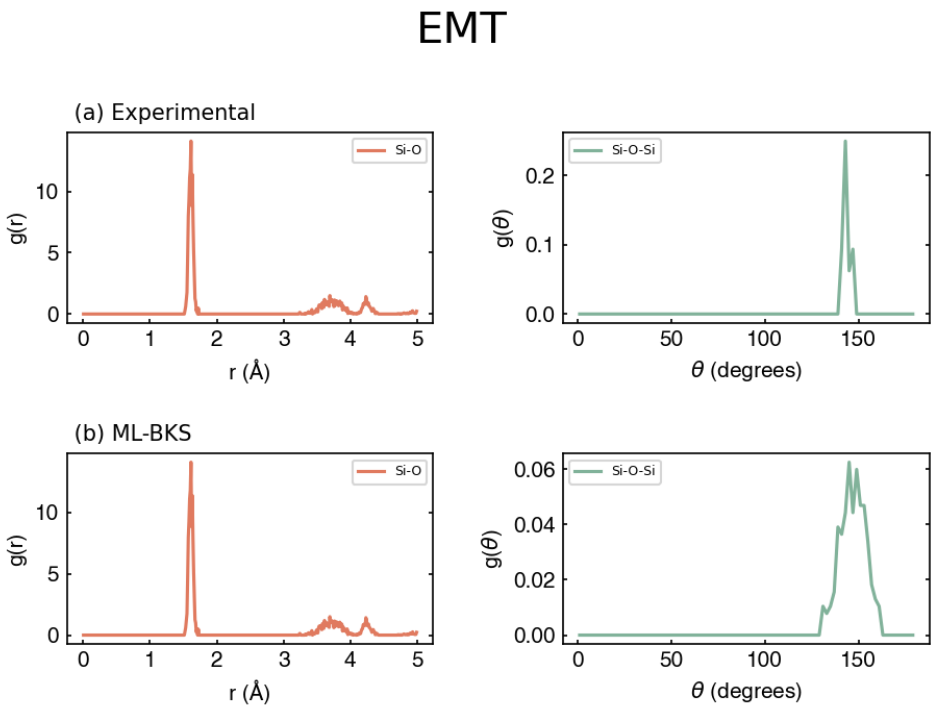

Supplementary Figure 23: Comparison of Si-O Bond Distance and Si-O-Si angle distribution from experiments and ML-BKS predictions for EMT

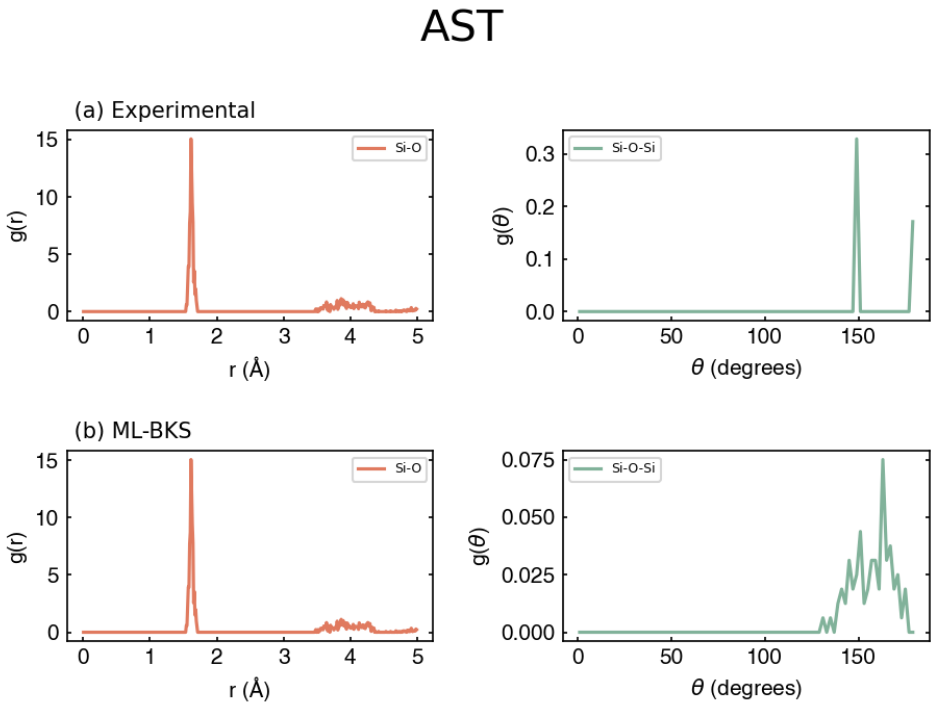

Supplementary Figure 24: Comparison of Si-O Bond Distance and Si-O-Si angle distribution from experiments and ML-BKS predictions for AST

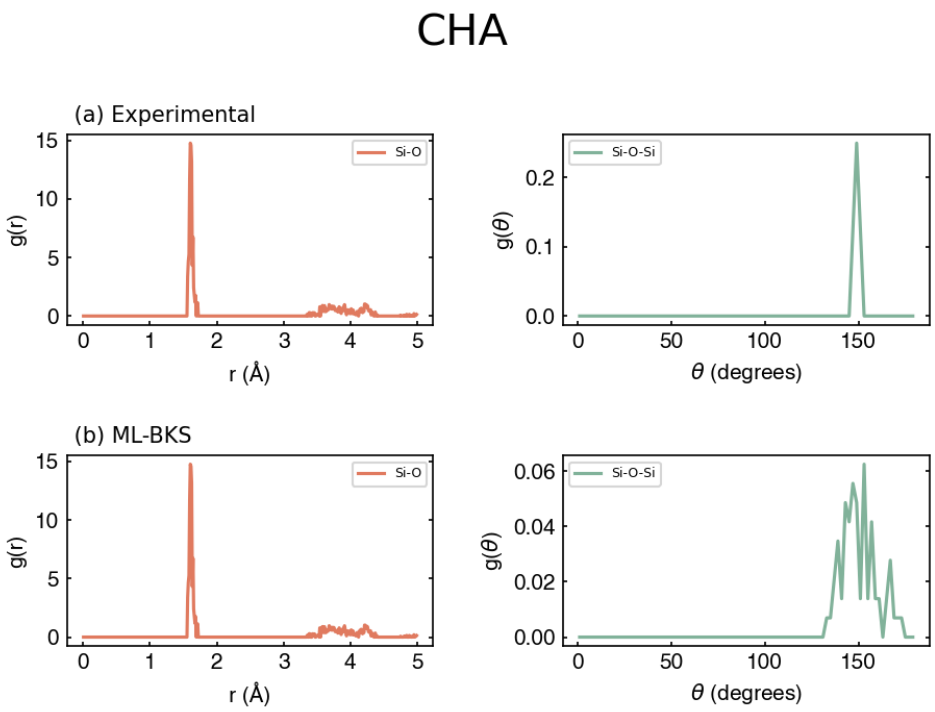

Supplementary Figure 25: Comparison of Si-O Bond Distance and Si-O-Si angle distribution from experiments and ML-BKS predictions for CHA

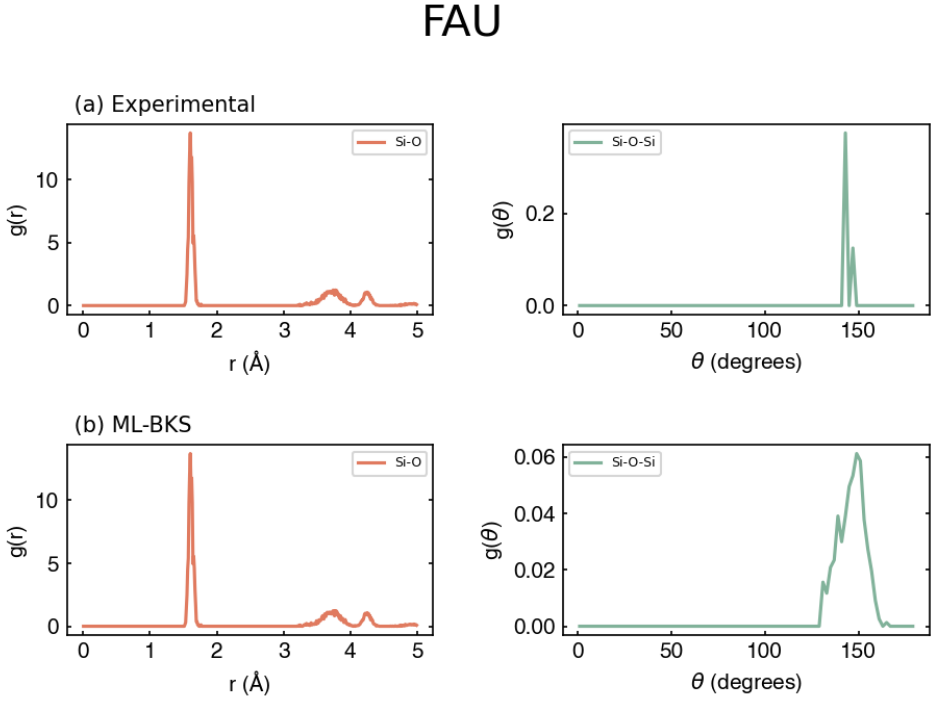

Supplementary Figure 26: Comparison of Si-O Bond Distance and Si-O-Si angle distribution from experiments and ML-BKS predictions for FAU

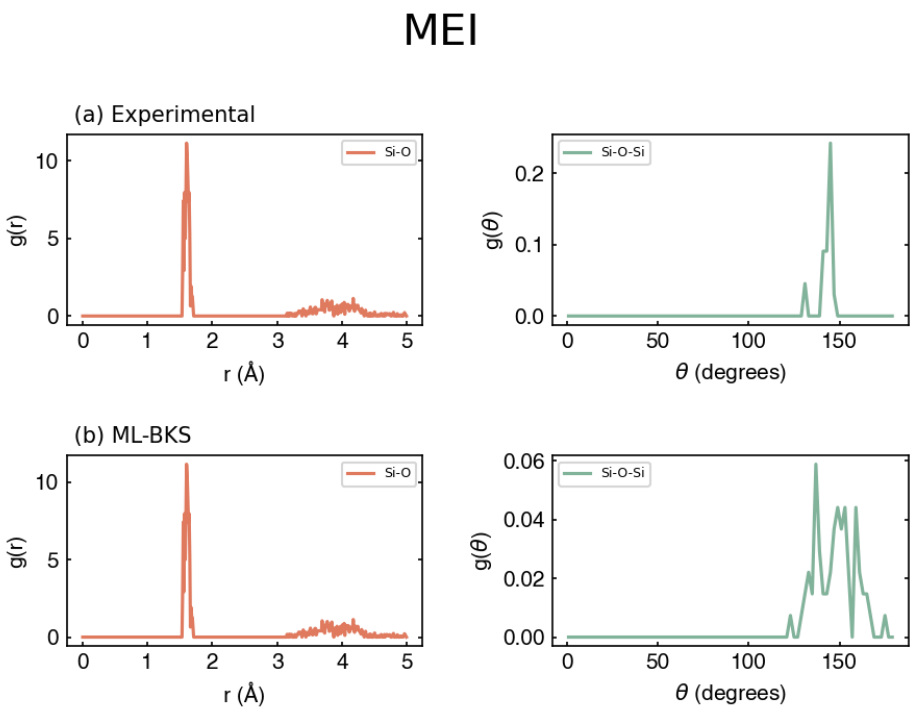

Supplementary Figure 27: Comparison of Si-O Bond Distance and Si-O-Si angle distribution from experiments and ML-BKS predictions for MEI

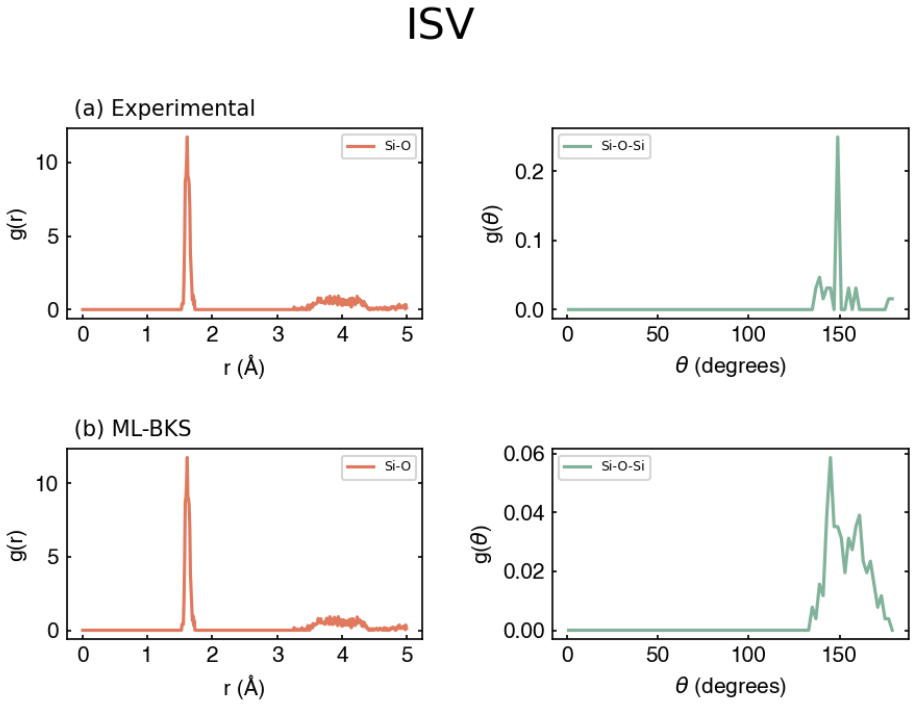

Supplementary Figure 28: Comparison of Si-O Bond Distance and Si-O-Si angle distribution from experiments and ML-BKS predictions for ISV

Supplementary Note 8: Performance between SLC and ML-BKS(this work)

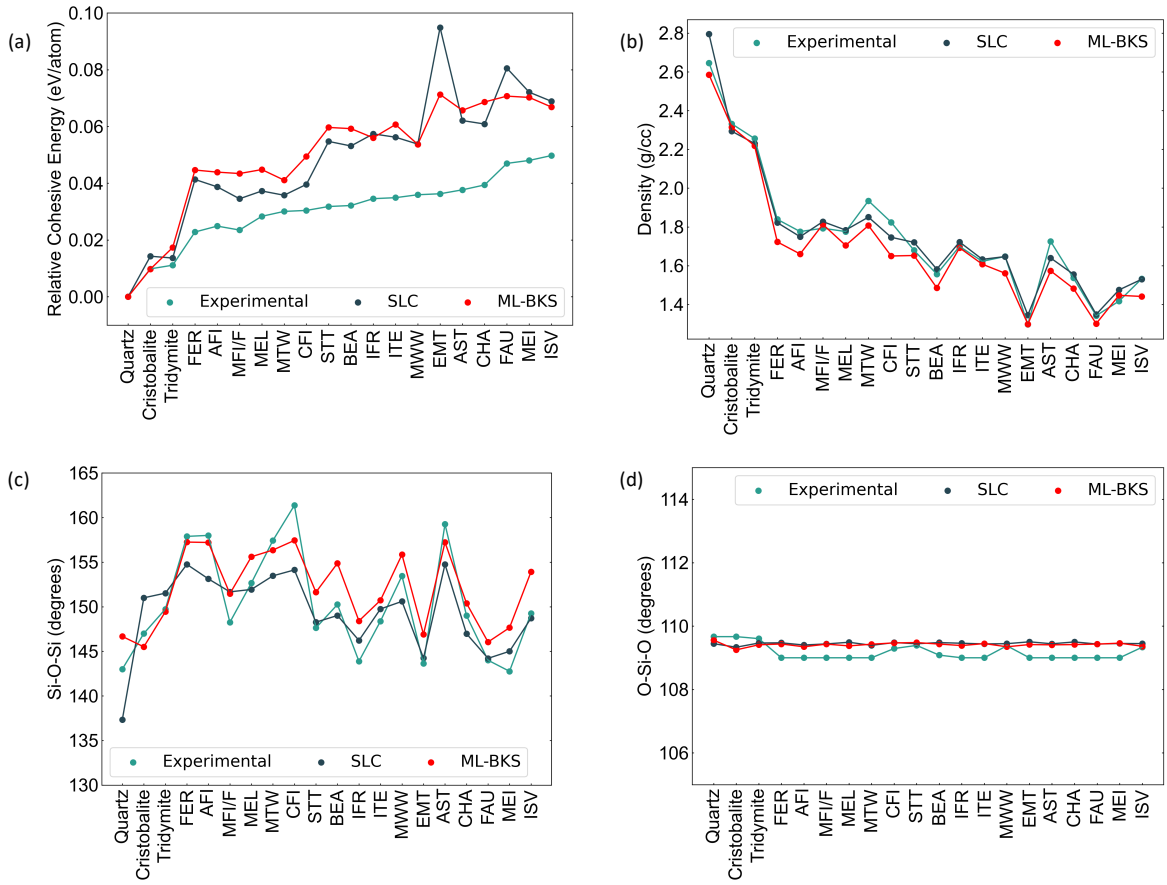

Supplementary Figure 29: Comparison of select properties and structural features of silica polymorphs predicted by different models. (a) Relative cohesive energy with respect to α-quartz, (b) Density, (c) Si-O-Si angle, (d) O-Si-O angle. All the properties were computed at 300K in order to compare with the reference experimental values. ML-BKS is the model developed in this work.

Supplementary Note 9: Comparison between Training & IZA database

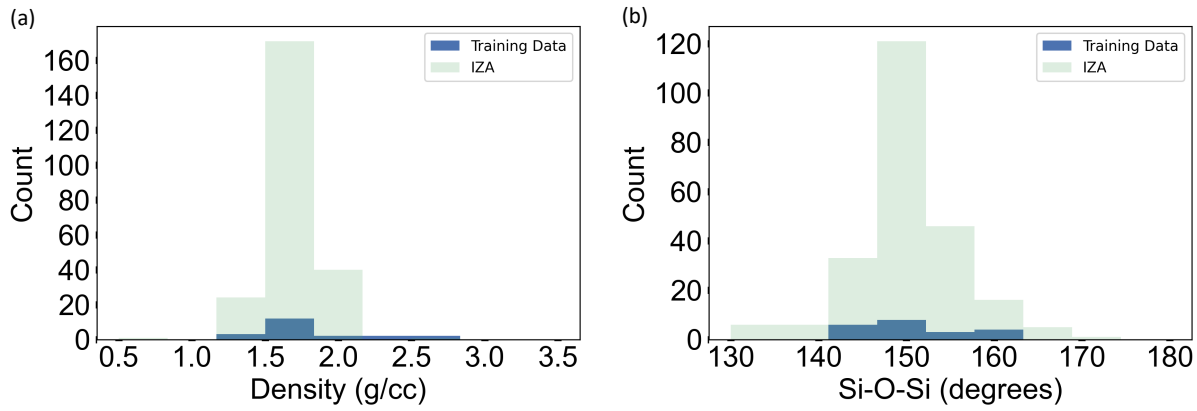

Supplementary Figure 30: Comparison of Si-O-Si and density ranges between the training set and IZA database

We can observe the width of the density training distribution is overlapping with the IZA database while the angular distribution suggests the training data to be a subset of the IZA polymorphs. But it is also noteworthy that they correspond to less than 10 percent of the dataset.

Supplementary References

[1] Sukriti Manna, Troy D Loeffler, Rohit Batra, Suvo Banik, Henry Chan, Bilvin Varughese, Kiran Sasikumar, Michael Sternberg, Tom Peterka, Mathew J Cherukara, et al. Learning in continuous action space for developing high dimensional potential energy models. *Nature Communications*, 13(1):1–10, 2022.